Journal of Materials Research and Technology 40 (2026) 3382–3399

Contents lists available at ScienceDirect

Journal of Materials Research and Technology

journal homepage: www.elsevier.com/locate/jmrt

Mechanical and microstructural properties of Ti–6Al–4V hybrid parts produced by LPBF: effect of deposited geometry and laser power

D. Palmeri, G. Pollara *, G. Buffa, L. Fratini

Department of Engineering, University of Palermo, Viale delle Scienze, 90128, Palermo, Italy

ARTICLE INFO

Keywords:
Hybrid parts
Ti–6Al–4V
LPBF
Numerical simulation
ANOVA

ABSTRACT

Hybrid Additive Manufacturing combines the high productivity of forming processes with the design freedom and customization of additive manufacturing. This study investigates the mechanical performance of hybrid components consisting of L-PBF features deposited on Ti–6Al–4V sheets under different process conditions. Because the integrity of the bonding interface is critical for the structural reliability of hybrid parts, the bonding strength was evaluated by means of three-point bending tests, macrostructural and microstructural analyses, and microhardness measurements. The distortions of the geometries along the building direction were also quantified and used to validate a numerical model of the L-PBF process on the metal sheet. The analysis revealed significant interactions among the process parameters, as identified through ANOVA. These interactions enabled the definition of two characterization parameters for the additive parts that are independent of the specific geometry considered. One is an index to quantify the symmetry of the deposited surface (IoS), and the other is to evaluate the heat accumulation (HA_V). The results demonstrate that the interface area and the symmetry of the additive part are the dominant factors controlling the mechanical strength of the hybrid component, through their effect on the residual stress distribution after processing. Based on these findings, a second-degree polynomial model was developed as a practical decision-making tool for selecting geometric and process parameters that ensure the required bonding strength in hybrid parts.

1. Introduction

In recent years, industries have been trying to produce more personalized products to meet customer needs [1–4]. At the same time, maintaining high productivity is necessary to remain competitive [5,6].

Nomenclature

AM	Additive Manufacturing
AP	Additive Part
D	Diameter
FEM	Finite Element Method
H	Height
HAM	Hybrid Additive Manufacturing
IS	Interface Surface
L	Length
LED	Line Energy Density
L-PBF	Laser Powder Bed Fusion
MAE	Mean Absolute Error
P	Laser Power
PRM	Parameter File
s	Scan speed
V	Volume
IS	Interface Surface (deposited AM surface)
Per	Perimeter of the IS
IoS	Index of symmetry for the IS
HA_V	Index of heat accumulation

The only way to meet both goals is through mass customization, where customers can ideally have a customized product at the same cost as a mass-produced part [7]. However, mass customization cannot be achieved by conventional manufacturing processes or additive manufacturing (AM) technologies [8]. On the one hand, conventional manufacturing processes, such as forming or casting, can be used for mass production but lack flexibility. On the other hand, AM technologies allow high flexibility but at the cost of productivity [9]. In this frame, hybrid manufacturing can be adopted to overcome the limitations of single processes and meet market needs [10]. The idea behind hybrid

* Corresponding author.
E-mail address: gaetano.pollara@unipa.it (G. Pollara).

https://doi.org/10.1016/j.jmrt.2026.01.042
Received 1 December 2025; Received in revised form 5 January 2026; Accepted 6 January 2026
Available online 8 January 2026

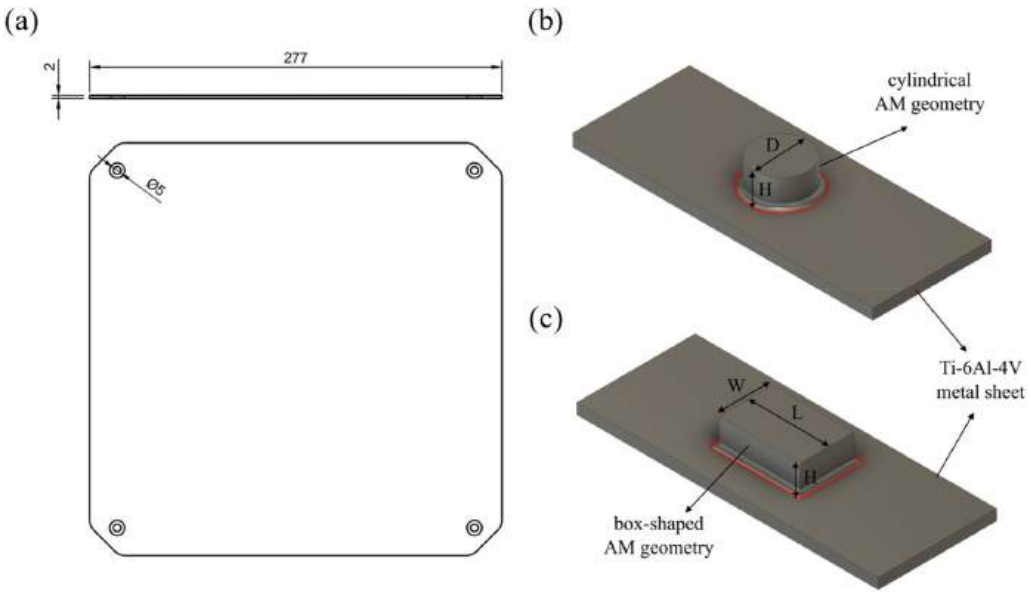

Fig. 1. (a) 2D sketch of the metal sheet used in this study. AM geometries printed on the metal sheet: (b) cylindrical and (c) box-shaped samples for the three-point bending tests samples. The interfaces between AM parts and metal sheets are highlighted with a red line.

Table 1
Samples with cylindrical AM geometry.

Sample ID	P (W)	LED (J/mm)	H (mm)	D (mm)	IS (mm^2)	V (mm^3)
1c	250	0.18	5	8	50	251
2c	250	0.18	5	10	79	393
3c	250	0.18	7	8	50	352
4c	250	0.18	7	10	79	550
5c	300	0.21	5	8	50	251
6c	300	0.21	5	10	79	393
7c	300	0.21	7	8	50	352
8c	300	0.21	7	10	79	550
9c	350	0.25	5	8	50	251
10c	350	0.25	5	10	79	393
11c	350	0.25	7	8	50	352
12c	350	0.25	7	10	79	550

Table 2
Samples with box-shaped AM geometry.

Sample ID	P (W)	LED (J/mm)	H (mm)	L (mm)	IS (mm^2)	V (mm^3)
1p	250	0.18	5	15	150	750
2p	250	0.18	5	20	200	1000
3p	250	0.18	7	15	150	1050
4p	250	0.18	7	20	200	1400
5p	300	0.21	5	15	150	750
6p	300	0.21	5	20	200	1000
7p	300	0.21	7	15	150	1050
8p	300	0.21	7	20	200	1400
9p	350	0.25	5	15	150	750
10p	350	0.25	5	20	200	1000
11p	350	0.25	7	15	150	1050
12p	350	0.25	7	20	200	1400

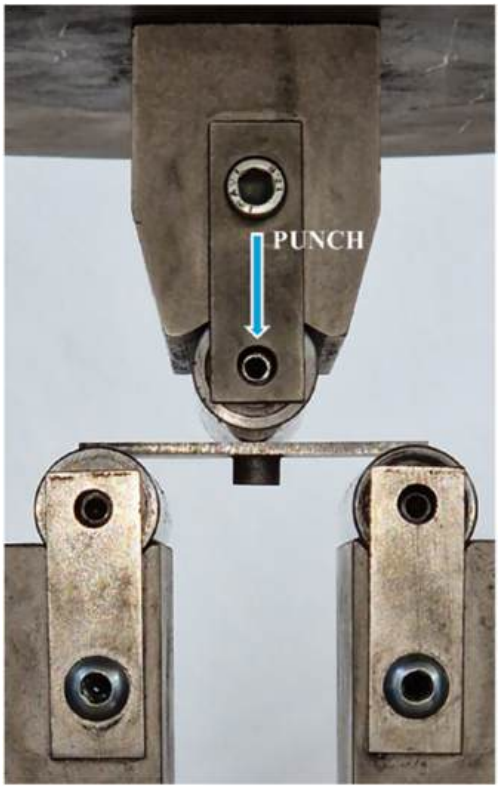

Fig. 2. Three-point bending tests set up.

techniques is to combine two or more processes and use the advantages of one to overcome the limitations of another [11,12]. Particularly, the combination of AM with other metal-forming processes shows promising results in terms of manufacturing time and cost per part [13,14]. The AM and forming processes can be combined in two ways: (i) the AM part can be printed on an already formed sheet, or (ii) the AM part can be applied to a sheet or bulk part and then formed [15]. Powder Bed Fusion (PBF) and Direct Energy Deposition (DED) are among the most used AM technologies for these applications [16–18]. In the PBF process, the heat source (laser or electron beam) is activated after the powder bed deposition, while, for the DED process, the material, in the form of powder or wire, is directly applied to the processing area [19]. For this reason, PBF is usually performed before the forming process, while DED can be easily carried out either before or after the forming step [20]. In the case of hybrid sheet parts, Laser Powder Bed fusion (L-PBF) is usually performed on the metal sheet before forming to locally increase its strength or add functional elements [21,22]. When process mechanisms

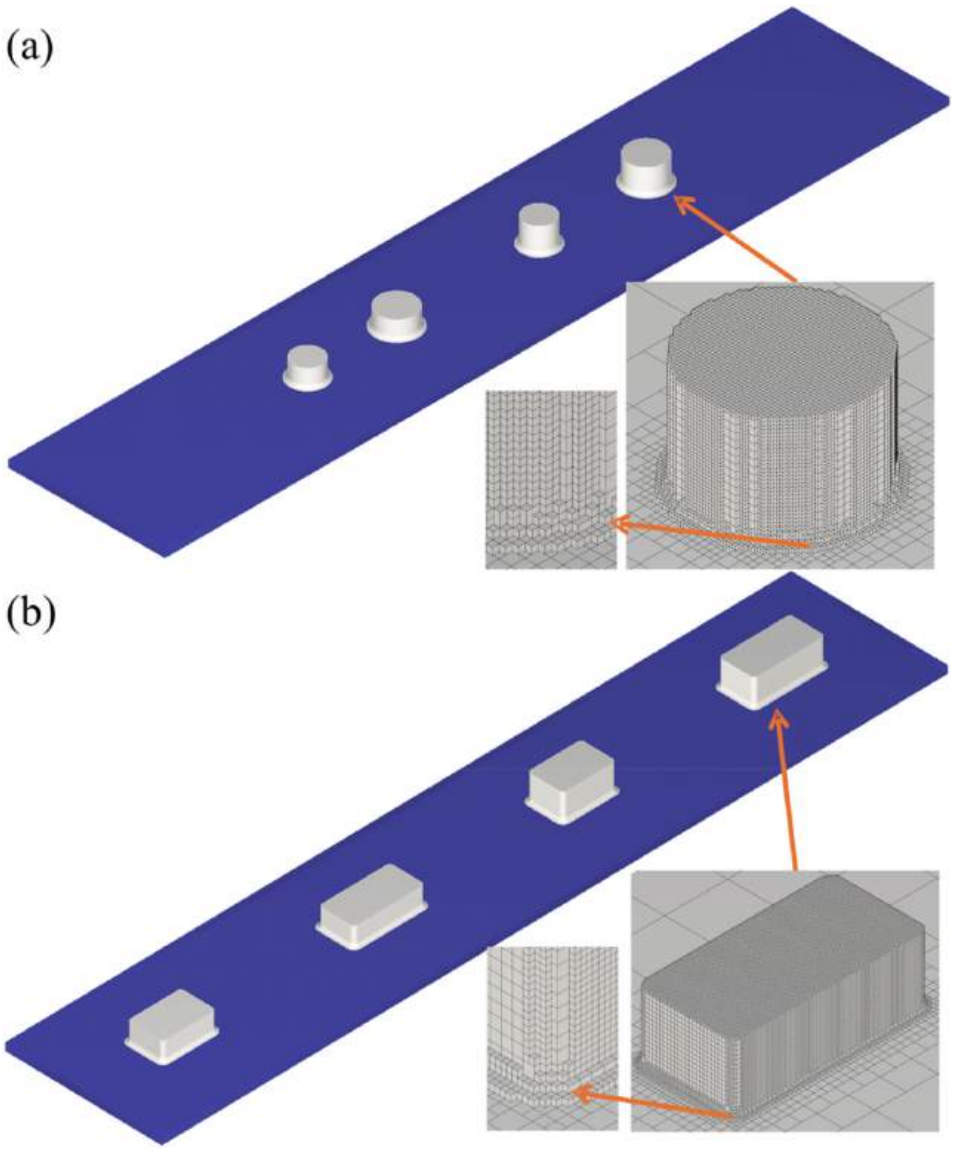

Fig. 3. Geometries and mesh used for the numerical simulations: (a) cylindrical and (b) box-shaped geometries. Details about the used voxel mesh are shown in the bottom-right corner of the images.

are sequentially applied, both processes will strongly influence the final part [23]. Hybrid manufacturing processes integrating DED with sheet metal forming have been developed to overcome limitations in surface quality, geometric precision, and mechanical properties of standalone additive manufacturing. Papke et al. [24]) introduce an alternating DED-LB/M and bulk forming approach using a fully integrated system with 316L stainless steel, primarily to smooth rough DED surfaces (reducing Rz by up to 50 %), adapt geometry via material flow, and enhance hardness through work hardening, enabling functional surfaces and near-net-shape parts superior to as-built AM structures. Similarly, Chen et al. [25] employ laser-powder DED on SS304 sheets to create reinforcement structures for stiffness enhancement in incremental forming, leveraging induced thermal stresses for shape alteration and distortion control in thin-walled components via optimized scan paths. Bambach et al. [26] utilize DED post-sheet forming, such as hole-flanging on AA6016, to locally reinforce components like deep-drawn cups, significantly increasing load-bearing capacity while minimizing tool needs for small-series production. These studies collectively demonstrate the combination's utility for surface finishing, distortion mitigation, and targeted stiffening in hybrid metal parts. Only a few studies on the interaction between the L-PBF and sheet metal forming processes can be found in the literature. Hafenecker et al. [27] analyzed the influence of substrate heating on the microstructural and mechanical properties of both materials. Since the substrate heating does not produce a visible effect on the material properties, it can be used to reduce residual stresses and thermal distortions. Ahuja et al. [28] focused on the fabrication of Ti–6Al–4V cylindrical additive-manufactured structures on a Ti–6Al–4V sheet. The interaction zone between the AM structure and the metal sheet was characterized through shear tests. The fillet's importance in reducing stress concentration and increasing the shear strength of the hybrid part was demonstrated. Moreover, they compared the shear strength of the hybrid part by applying the AM structure on a flat and deep-drawn sheet. Schaub et al. [29] studied the influence of the energy input during the deposition on the bonding zone using the same geometry as the previous study. Providing too-low or too-high energy resulted in insufficient bonding and high porosity, leading to low shear strength. Although it is well established that geometrical factors can significantly affect the mechanical and microstructural properties of parts produced by LPBF, as they influence the thermal flow inside the part and towards the backplate [30], the literature review highlights a lack of knowledge in the analysis of the influence of the specific geometric characteristics of

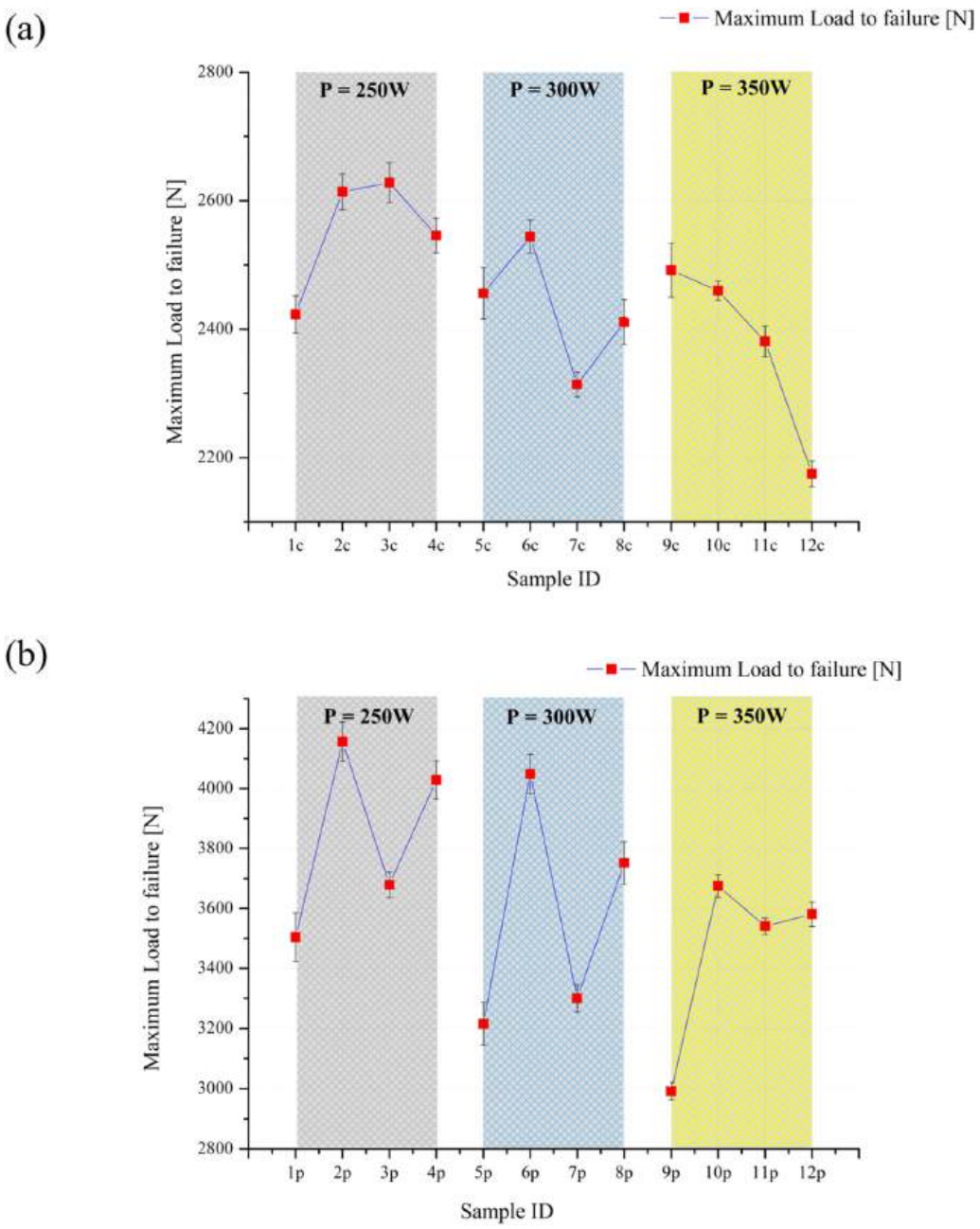

Fig. 4. Bending test results: Maximum load to failure [N] for the (a) cylindrical and (b) box-shaped AP.

the Additive Part (AP) on the effectiveness of the hybrid components for subsequent part forming. In this paper, two different geometries were considered for the production of an AP on a Ti–6Al–4V sheet, i.e., cylindrical and box-shaped, printed using Laser Powder Bed Fusion (L-PBF) technology on a sheet metal. The strength of the transition zone between the sheet metal and the AP was characterized in terms of formability by three-point bending tests in tension configuration [31], as the Volume (V), Interface Surface (IS) between the AP and the sheet, and the height of the AP varied. The macro and microstructural analysis of the transition zone was carried out, highlighting the occurring remelting phenomena. A three-way ANOVA was carried out to assess the significance of the individual main factors (Power, Height, and Diameter/-Length) and their interactions, both double and triple, concerning the formability and residual stresses of the transition zone of the APs. Finally, a numerical model of the hybrid additive process was developed, using the Netfabb software, to predict the residual stress distribution. The distortions along the z direction (building direction) were measured, and the values were used to validate the numerical model. The results were used to identify the most influential parameters and to develop a general model to predict, regardless of the part geometry, the part's mechanical response in terms of maximal flexural strength, as an indicator of the interface bonding strength. The proposed model can be used as a decision-making tool for engineers during the design phase of hybrid parts.

2. Materials and methods

2.1. Experimental setup

In the Hybrid Additive Manufacturing (HAM) frame, the L-PBF was performed on a metal sheet. A Ti–6Al–4V metal sheet with dimensions 277 mm × 277 mm x 2 mm (Fig. 1 (a)) was fixed on a 280 mm × 280 mm

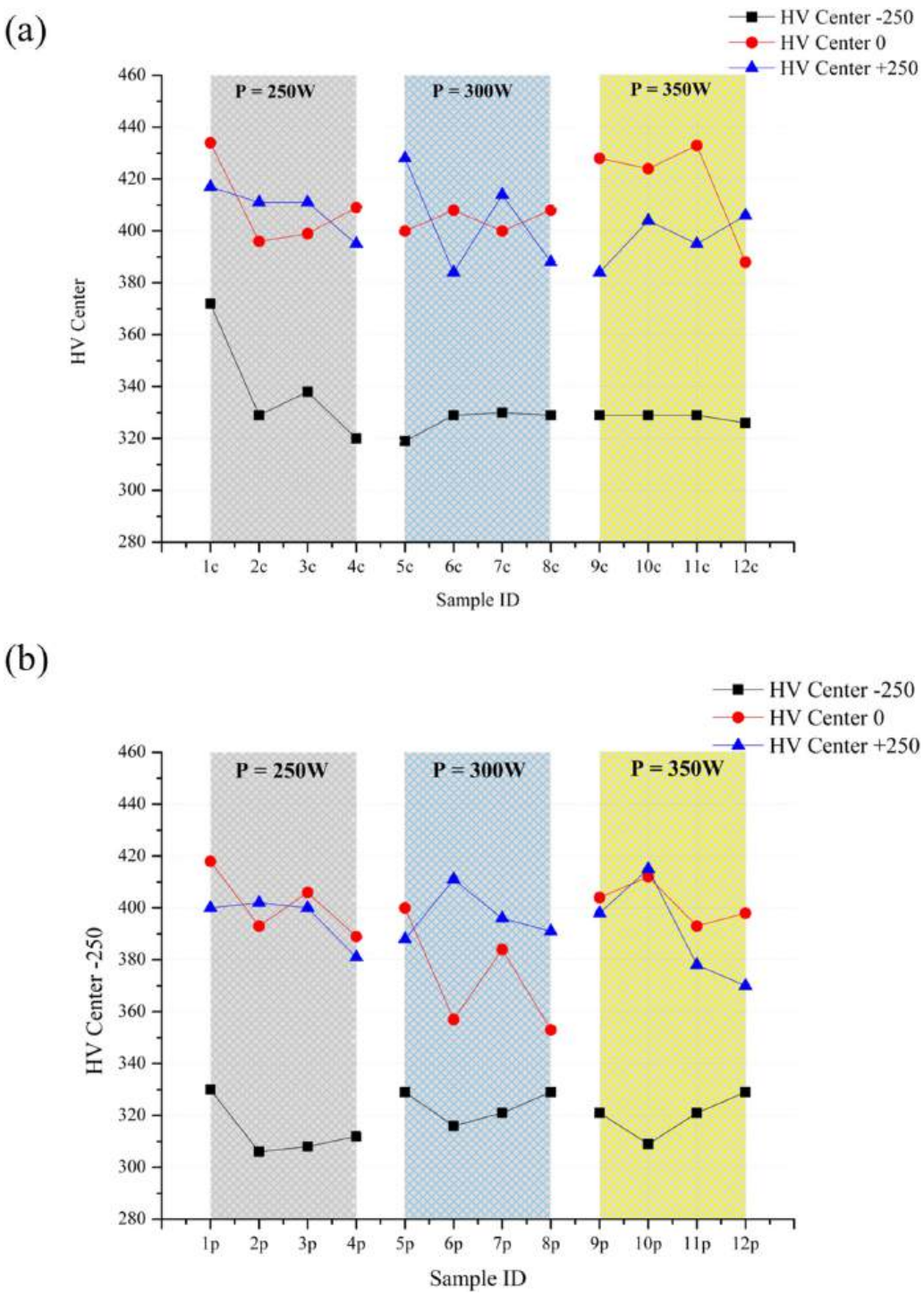

Fig. 5. Microhardness results for (a) cylindrical samples and (b) box-shaped samples.

x 25 mm build plate of the same material. Four holes, 5 mm in diameter, were drilled at the corners of the metal sheet to allow the placement of four flathead screws to fix it to the build plate. The L-PBF process was used to print two different geometries: a box-shaped and a cylindrical one (Fig. 1(b) and (c)). A SLM 280 HL (Nikon SLM Solutions AG, Belgium) 3D system machine was used to selectively melt Ti–6Al–4V spherical powder with a mass density of 4.43 g/cm^3 and a dimension of 23–60 μm. The build chamber was filled with argon to lower the oxygen level to 0.1 % to avoid powder oxidation. Moreover, the built plate temperature was set to 200 °C to reduce thermal gradients and residual stress [32]. For each sample, laser speed (s), hatch spacing (h), and layer thickness (l) were kept constant and equal to 1400 mm/s, 120 μm, and 30 μm, respectively. Three different levels of laser power (250 W, 300 W, and 350 W) were selected, resulting in samples with a linear energy density (LED = P/s) of 0.18 J/mm, 0.21 J/mm, and 0.25 J/mm. The process parameters were chosen according to previous studies reported in the literature on the same material [33,34]. The two features were fabricated with different combinations of geometrical parameters, i.e., height (H) and diameter (D) for cylindrical samples, and height (H) and length (L) for box-shaped samples. The different samples for cylindrical and box-shaped geometries are reported in Tables 1 and 2, respectively. In detail, AM geometries were printed with an H equal to 5 mm or 7 mm.

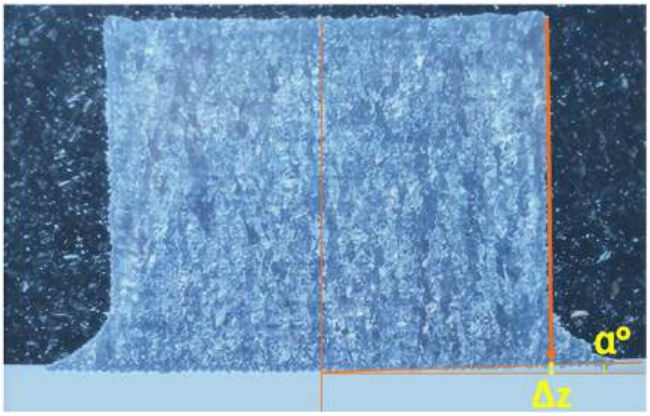

Fig. 6. Cross-section of the hybrid part highlighting the method used for the measurement of the distortion Δz (mm).

Also, two levels of D (8 mm and 10 mm) and L (15 mm and 20 mm) were chosen. The width (W) of the box-shaped geometries was fixed at 10 mm. A fillet radius equal to 1 mm was used for all the geometries to reduce stress concentration. Four specimens were printed for each ID. The geometric parameters of the current study were selected to assess the impact of many variables connected to the production of these geometries using additive technology, starting from the dimensional values specified in the literature, referring to the production of functional elements [11,27]. In particular, the additive part's height, diameter, and/or interfacial surface area were varied in order to examine the impact of heat accumulation phenomena resulting from the significant increase in the additive part, as well as the impact of the interfacial surface area's extent and geometric symmetry on the strength of the interfacial zone between the substrate and the additive part. Three-point bending tests were carried out to study the mechanical properties of the hybrid structures. To this aim, the metal sheet was cut to obtain samples of 56 mm × 22 mm x 2 mm, as shown in Fig. 1. A Galdabini Quasar 600 universal testing machine was used with a constant speed of 0.5 mm/min. For each case study, three samples were tested, while the fourth was used for the microstructural analysis. The three-point bending test was conducted maintaining the AP on the side subjected to tension during the test, as shown in Fig. 2. Samples underwent standard metallurgical preparation consisting of grinding and polishing, followed by etching with Kroll's reagent for 30 s. An Olympus G1 optical microscope was used to observe the bonding area between the metal sheet and the AM part. The samples examined by the optical microscope were further characterized by investigating the transition zone between the additive part and the substrate using a Phenom ProX SEM microscope. The transition zone was also subjected to Energy Dispersive X-ray Spectroscopy (EDX) investigation to identify the distribution of the elements titanium, aluminium, and vanadium. Finally, Vickers microhardness tests were carried out along a vertical line in the center of the sample cross-section. Each indentation was spaced 250 μm, both above and below the sheet top surface (zero value).

2.2. Numerical simulation

Numerical simulations were conducted using the commercial software Netfabb Simulation (Autodesk) to study distortions along the building direction (z) and residual stress distributions after the L-PBF process (see Fig. 3). The developed FEM model is based on a multi-scale modeling approach where the analysis is split into multiple stages [35]. Particularly, three different steps were considered: (I) Modeling of the heat source at the micro-scale level; (II) Prediction of the local residual stress field in the mesoscale model starting from the thermal model obtained in the first stage; (III) Prediction of residual stress and part distortion at the macro-scale level by using the residual stress field from the mesoscale model. In this way, the mechanical response of the part in terms of distortions is obtained using the thermal history at the micro-scale as the input [36]. The part-level simulation requires low computation time since the thermal and mechanical analyses are weakly coupled. An adaptive mesh was used, which allowed for maintaining a finer mesh in regions subjected to significant thermal or displacement gradients for better accuracy, while adopting a coarser mesh in the other areas to reduce the computational time [37]. An 8-node hexahedral mesh was generated from the STL file, resulting in elements with an axis-aligned rectangular voxel mesh (Fig. 3). A hybrid activation strategy was used to model the AM process. With this method, elements are present from the start of the analysis but set as inactive. According to the deposition strategy, the elements within the layer are switched to quiet and then switched individually to active, reducing run times. To run the numerical simulation, it was necessary to specify the material properties, scan strategy, and machine parameters for the generation of the parameter file (PRM). The PRM file includes the information at the mesoscale level that will be used for the part-scale model. In this study, the voxel mesh was generated using seven layers per element; two sets of simulations were carried out: one with only the box-shaped and the other with only the cylinders, as shown in Fig. 3.

3. Results and discussion

3.1. Mechanical response of hybrid parts

Three-point bending tests and microhardness have been performed to characterize the mechanical behavior of hybrid parts. Moreover, the distortions after the L-PBF process on the sheet metal were measured to observe the effect of the residual stresses induced by the AM process. The results of three-point bending tests conducted on samples with cylindrical and box-shaped geometry are reported in Fig. 4(a) and (b), respectively, in terms of maximum load to failure [N]. It is worth noting that load and displacement are typically used to study the mechanical response in three-point bending tests, especially when it is difficult to evaluate flexural stress and strain [38,39]. The results of such tests provide useful qualitative indications for assessing the feasibility of performing sheet metal forming operations after the additive process. A progressive decrease in the strength at the interface of the hybrid sample is observed for cylindrical geometries as the LED, related to the additive manufacturing process, increases. The phenomena that must be considered for a more accurate understanding of three-point bending test results are related to the increase in IS and volume (V) of the AP. Increasing IS, for a given AP height, allows for greater heat exchange with the substrate during the process and facilitates the cooling of the part, increasing its strength. As the volume of the AP increases, the heat flow towards the sheet metal increases. It is worth noting that, for the lowest laser power value (P = 250W), increasing the H parameter for samples 1C and 3C does not result in a decrease of the interfacial resistance because of the greater remelting depth, as will be demonstrated in paragraph 3.2. For the intermediate laser power value (P = 300W), increasing the AP-sheet IS promotes greater thermal exchange between the AP and the sheet, increasing the maximum load to failure measured in the three-point bending test. Instead, increasing the volume of the AP due to a change in the H parameter increases thermal flow towards the sheet metal, promoting the formation of heat accumulation phenomena, as defined in Ref. [40]. Under such conditions, the interface between the AP and the sheet is characterized by lower strength. For high laser power value (P = 300W), the effect of the higher energy density prevails over all the geometric characteristics of the cylindrical APs. This results in a progressive reduction of the interface strength.

A progressive softening of the resistance at the interface of the hybrid sample is observed for the box-shaped geometries as the LED associated with additive manufacturing increases (Fig. 4b). On the other hand, for a fixed thermal input, the increase in the AP-sheet IS promotes the activation of higher thermal flows for heat dissipation. This phenomenon

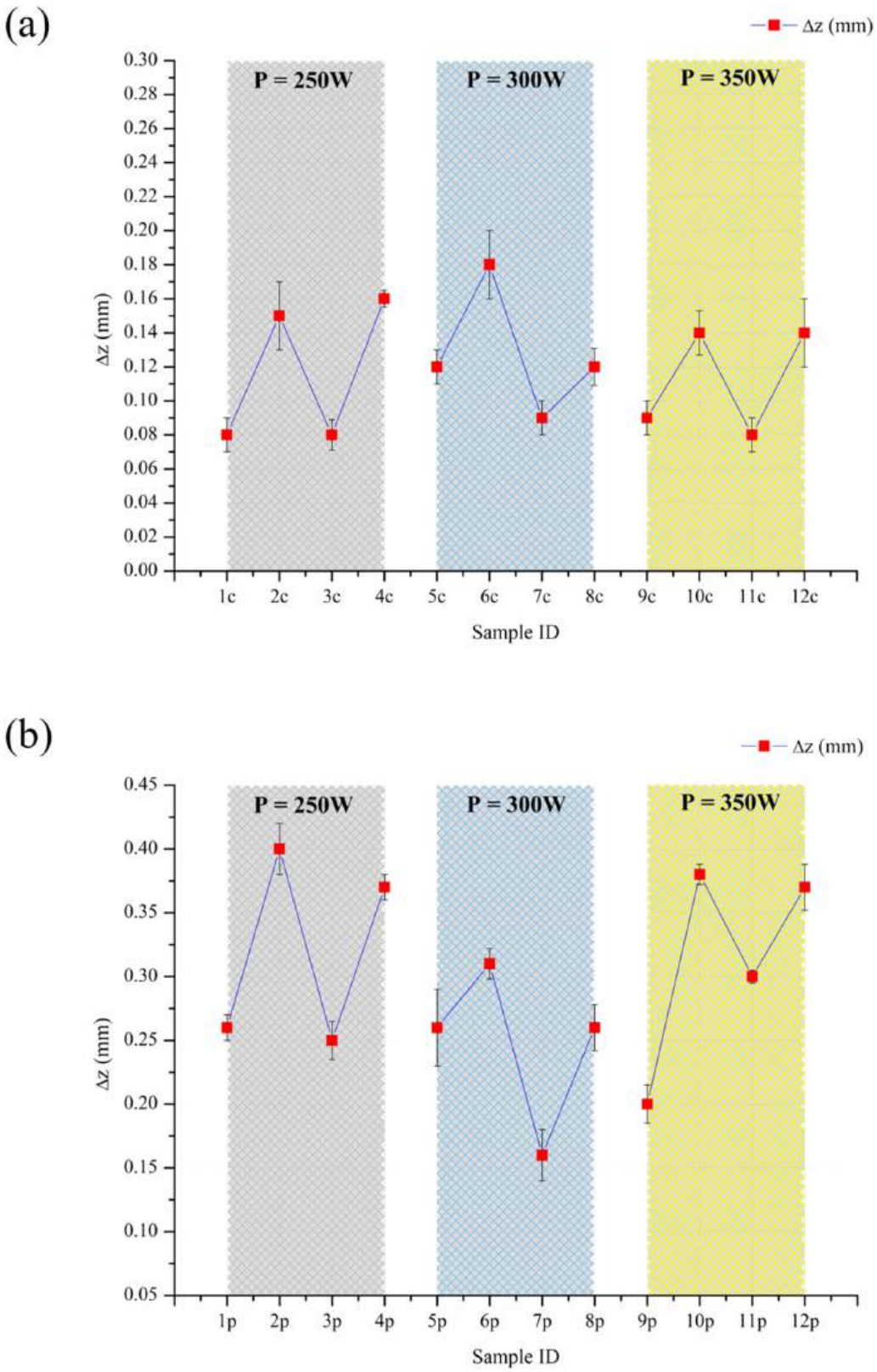

Fig. 7. Measured distortions Δz as the geometric parameters H and D and the laser power vary for (a) the cylindrical geometry, and (b) the box-shaped geometry.

results in greater resistance at the interface. The different behaviors of the cylindrical and box-shaped geometries can be explained as follows. When the volume of the AP increases at constant IS, the maximum load can be related to the degree of symmetry of the considered geometry and to the variations in residual stresses that arise as a consequence of the additive process. As will be discussed in the following, when the length-to-width ratio of the interface surface is higher, the concentration of stresses along the shorter sides of the perimeter is higher, and the resistance of the AP decreases.

Preliminary microhardness analyses on hybrid samples showed that

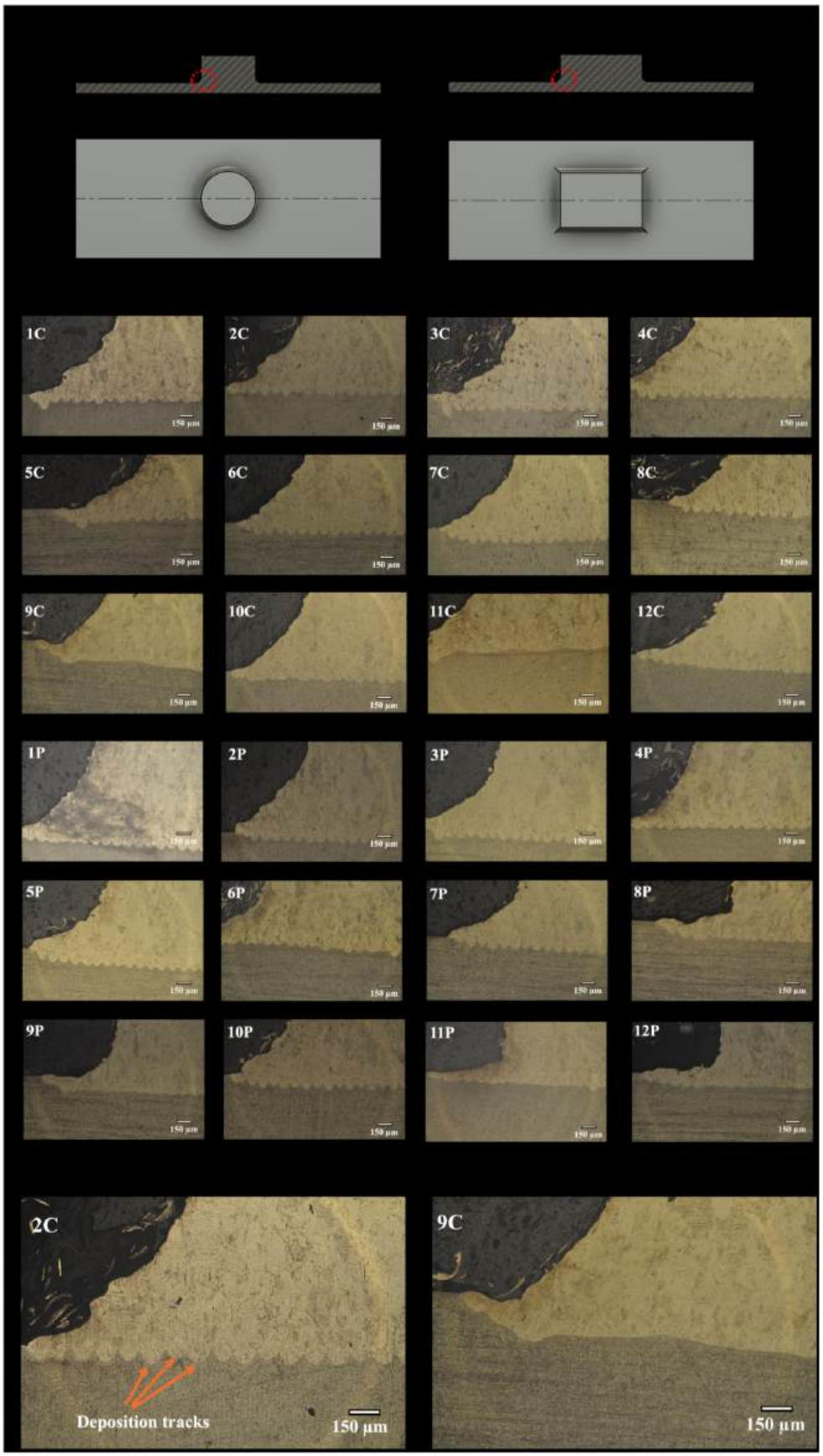

Fig. 8. (a) Sketch of the observed section, fillet area is highlighted with a dashed red line. (b) Microstructure of the hybrid interface zone near the fillet of the AP geometries. (c) Laser tracks at the interface for sample 2C (P = 250 W). (d) Remelting of the first deposited layers for sample 9C (P = 350 W).

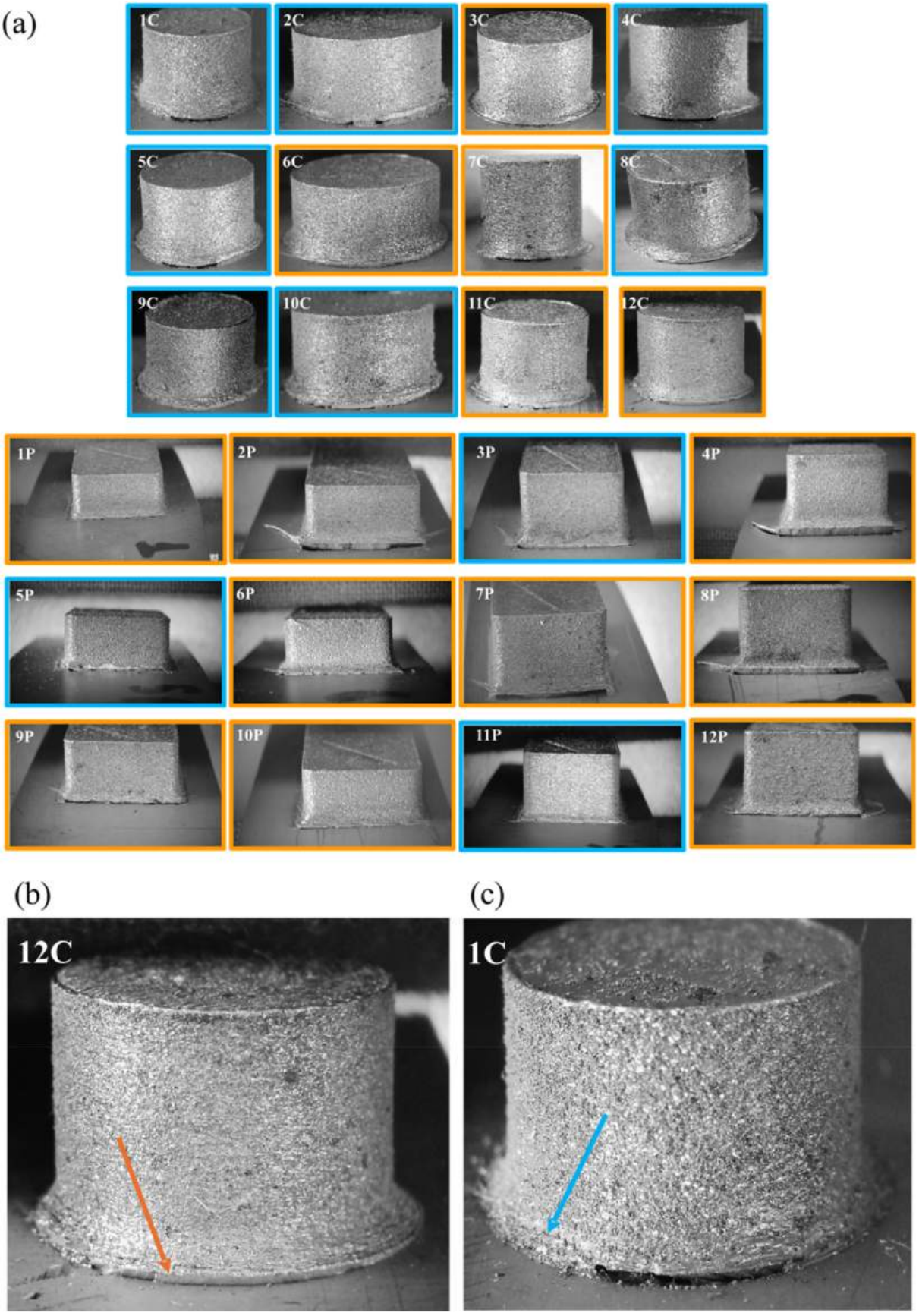

Fig. 9. Macrographs of the fracture zones of the samples subjected to three-point bending tests: (a) All the fractured samples (cylindrical and box-shaped). samples for which the failure began at the base of the fillet orange box and samples for which the failure began on the fillet blue box, (b) Sample 12C in which the fracture started at the base of the fillet; (c) Sample 1C in which the fracture started in the fillet area.

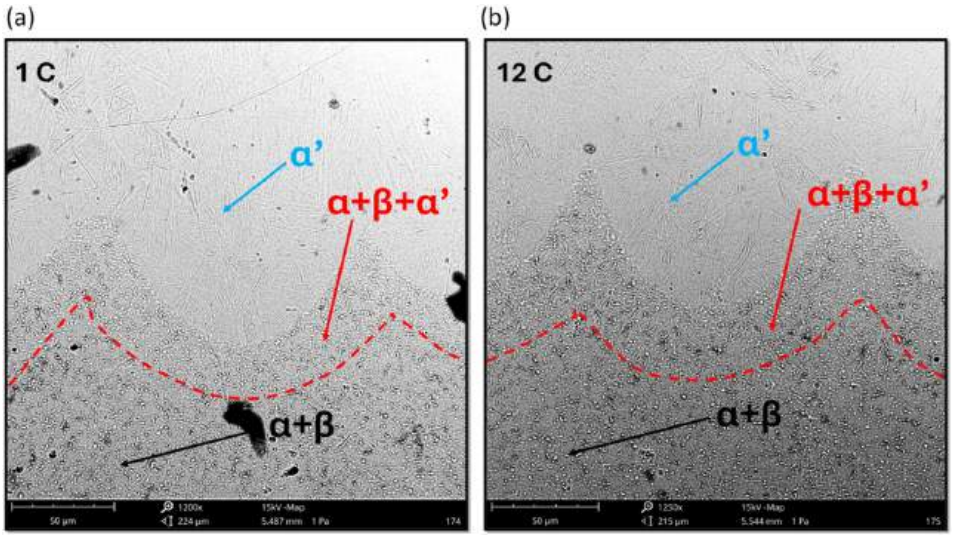

Fig. 10. Micrographs of the transition zones of the samples: (a) Sample 1C in which inside the α+β+α′ region there is a lower segregation of V-rich phase β; (b) Sample 12C in which inside the α+β+α′ region there is a higher segregation of V-rich phase β.

HV values stabilize at distances greater than 250 μm from the interface. Hence, Fig. 5 (a) and (b) show the results of the microhardness tests only up to distances of 250 μm from the interface. For the cylindrical APs, the microhardness results show that for all the analyzed LED values, the interface's microhardness reflects the AP's microhardness. Regarding the sheet, however, the microhardness values show that for P = 250 W, the hardness decreases when the thermal flux from the AP towards the sheet metal increases, i.e., for the 2C, 3C, and 4C samples. For higher P values, the softening of the sheet is independent of the variation in thermal flux. As for the box-shaped samples, the interface's microhardness is similar to the additive part's microhardness even when the thermal flows between the AP and sheet metal vary. For this geometry, all examined power values generate sheet softening. This phenomenon is attributed to the fact that the IS are larger than the ones in the cylindrical geometries. The hardness values obtained in this study are comparable to those reported in the literature by Papke et al. [31]. Similarly, the progressive increase in hardness observed from the sheet metal substrate to the additively manufactured element aligns closely with their findings, further validating the material behavior under hybrid processing conditions.

The acquired macrographic images were used to determine the distortions in additive geometries along the z-direction. The pictures were imported into CAD modeling software, and the distortion angle of the sample was measured in the z direction by placing the origin of the angular measurement on the vertical symmetry axis of the additive geometry section. After calculating the distortion angle and taking into account the geometric parameters of the AP, the distortion value (Δz) at the fillet end of the AP was determined, as highlighted in Fig. 6.

Fig. 7 shows the Δz parameter as a function of the laser power and parts geometry. For the cylindrical geometries, the distortions appear weakly dependent on the LED during the additive process, as the distortion trends are similar for increasing powers. As expected, the distortions are more significant in the samples where the IS parameter is higher. For low LED values, the distortions are not influenced by the increase in AP height. The same observation applies to the case of high LED values. On the other hand, the increase in the height of the AP produces a decrease in distortions for intermediate LED values, due to a more favorable residual stress distribution (paragraph 3.3). Fig. 7 (b) illustrates the correlation between distortions, geometric parameters, and power for the box-shaped AP.

The increased extent of the IS and the decreased axial symmetry of the interface geometry led to a sensitivity of the distortions to the LED value due to the additive process. This is because of the different distribution of thermal fluxes and residual stresses, which are strongly affected by IS and LED values, as will be better highlighted in the following paragraph. The intermediate LED value and the geometry defined by a low IS value and a high H value achieve the lowest distortions. The bending test, microhardness, and distortion results indicate that the individual main factors, whether geometric or process-related, fail to comprehensively explain the variability of the results. For this reason, an ANOVA analysis was carried out to highlight significant double and triple interactions between the main factors and the measured variables (paragraph 3.4).

3.2. *In-depth analysis of the transition zone*

The analysis of the interface zone at the base of the AP (Fig. 8) reveals that the morphology of the interface is primarily determined by the power value used during the additive process. For high LED values, both cylindrical and box-shaped geometry samples exhibit a pronounced remelting zone at the interface between the additive part and the sheet metal. The pronounced remelting during the first layer deposition significantly impacts the microstructural morphology of the AP-sheet interface zone. The laser deposition tracks are detectable at the interface for P values of 250 W and 300 W, appearing adjacent to each other and spaced by an amount equal to the hatch spacing used (see Fig. 8 b). The single tracks associated with the additive deposition of the first layer are no longer distinguishable when P is set to 350 W due to the increased remelting of the first deposited layers. In general, the resistance of the interface is lower when the morphology of the IS exhibits a visible remelting effect of the first deposited layers, as can be inferred by comparing Figs. 4 and 8, in contrast to when the remelting is less pronounced. This is the case for both IS with high symmetry, i.e., circular, and IS with reduced symmetry, i.e., rectangular. The microstructural images of the APs fillet zone, representing the longitudinal section on the hybrid samples, also show that the fillet radius changes when pronounced remelting phenomena occur. This geometric modification affects how residual stresses are distributed in the joints. Fig. 9 displays the macrographic images of the fracture modes of the samples subjected to three-point bending tests. Two distinct fracture modes were identified in the cylindrical geometry samples. In one case, the fracture started at the base of the fillet between the additive part and the sheet metal and spread to the interface zone. In the second case, the fracture started in the fillet area and spread to the additive part before reaching the interface. The first failure mode was observed in samples 3C, 6C, 7C, 11C, and 12C (orange box in Fig. 9 (a)). The second mode of failure was observed in the remaining cylindrical geometry samples (blue box in

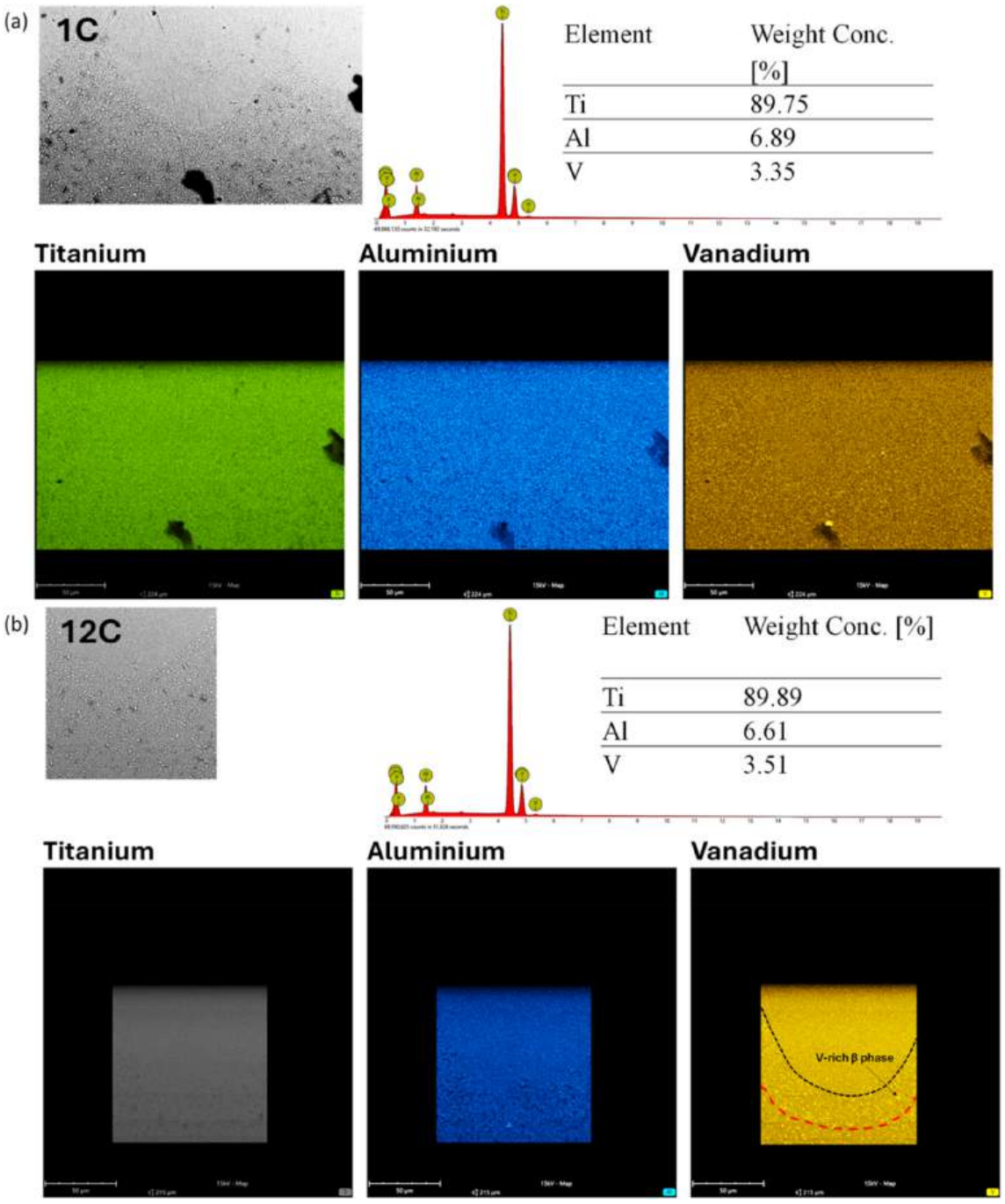

Fig. 11. EDX maps of the transition zones: (a) Sample 1C, in which inside the α+β+α′ region there is a lower segregation of V-rich phase β; (b) Sample 12C in which inside the α+β+α′ region there is a higher segregation of V-rich phase β.

Fig. 9 (a)). Two kinds of failure similar to the previous ones have also been observed for the AP with box-shaped geometry. In this case, the start of the failure at the base or within the fillet was observed on the shorter side of the box-shaped. The samples for which the failure began at the base of the fillet are 1P, 2P, 4P, 6P, 7P, 8P, 9P, 10P, and 12P (orange box in Fig. 9 (a)). The samples for which the failure began on the fillet are 3P, 5P, and 11P (blue box in Fig. 9 (a)). Overall, fracture initiation and consequent structural failure predominantly occur in proximity to the interface between the sheet metal substrate and the additively manufactured component, consistent with observations reported by Ahuja et al. [28].

A more detailed examination of the transition zone between the additively manufactured part (AP) and the substrate was carried out using scanning electron microscopy (SEM), as shown in Fig. 10. This analysis highlighted, inside the transition zone, a distinct microstructural gradient characterized by the presence of α+β+α′ phases. The region produced by additive deposition clearly displays a typical martensitic α' structure, which is commonly observed in Ti–6Al–4V processed by rapid cooling techniques such as laser powder bed fusion or directed energy deposition [30,31]. In turn, near the transition zone, the substrate retains the conventional α+β microstructure found in wrought Ti–6Al–4V sheets [34]. Within this gradient, the β phase (body-centered cubic, BCC) tends to localize at the boundaries of equiaxed α grains (hexagonal close-packed, HCP), similarly to what was observed in thermomechanically treated Ti–6Al–4V alloys [33,35]. A microstructural analysis was also conducted by Schaub et al. [29] to highlight the

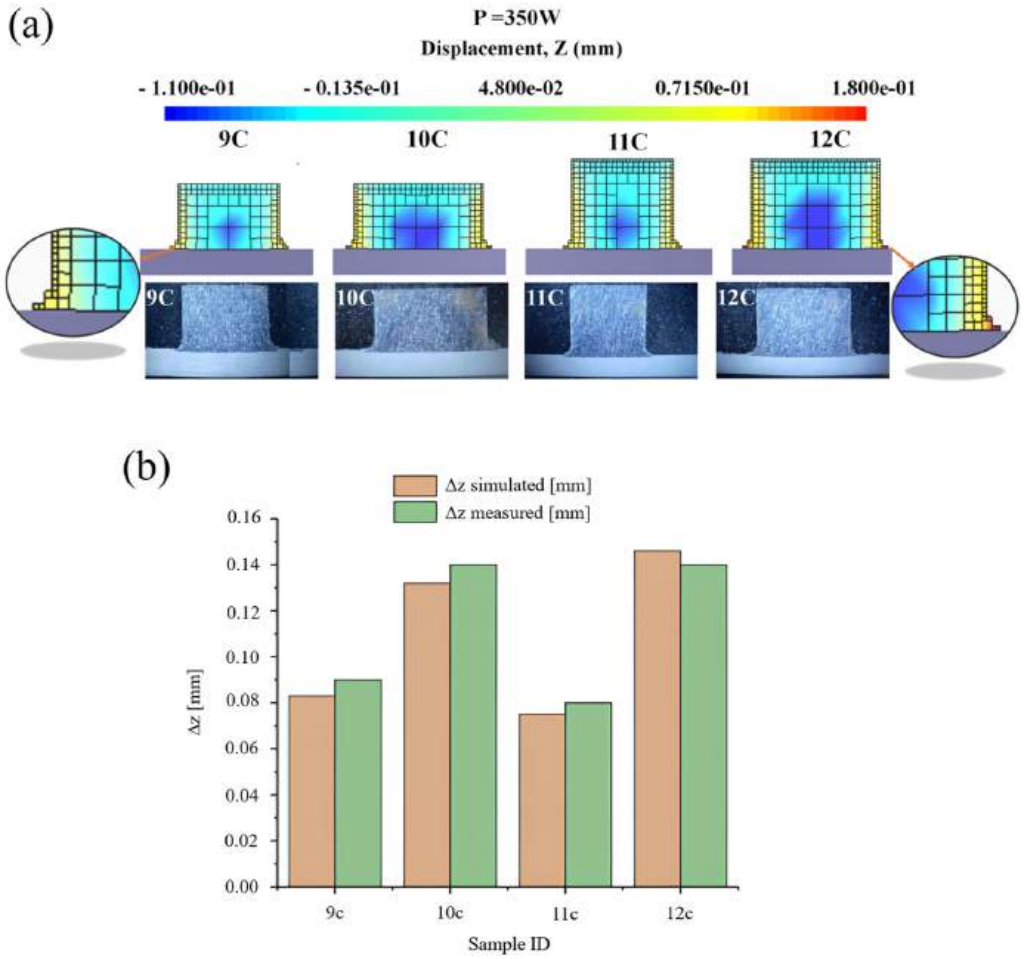

Fig. 12. (a) Displacements (ΔZ) obtained from the simulation model for cylindrical AP with P = 350W, (b) comparison between the measured displacement values and the simulated ones.

transition zone, which serves as an indicator of the interaction between the additively manufactured part and the initial sheet metal substrate. The energy input required to melt the powders and form the additive component induces microstructural changes within the sheet metal, thereby influencing its mechanical properties. Nevertheless, their study lacks a detailed examination of the transition zone to identify the specific phases present.

In order to obtain a more comprehensive qualitative characterization of the phase distribution in the transition zone between the AP and the substrate, a mapping analysis was performed using Energy Dispersive X-ray Spectroscopy (EDX). The EDX results are reported in Fig. 11, highlighting the differences in the distribution of elements in the transition zone between the molten zone (AP) and the substrate, comparing two operating conditions of the L-PBF process for Ti–6Al–4V alloys. In particular, a low power (P = 220 W, sample 1C) and a high power (P = 350 W, sample 12C) are considered. It is seen that the increase in laser power results in an increase in thermal flux and a consequent different distribution of alloying elements. High laser power results in a more pronounced segregation of the β phase, which preferentially concentrates along the edges of the equiaxed grains of the α phase. This segregation is favored by the decrease in local cooling rate and the consequent greater diffusion of alloying elements (especially vanadium), which stabilize the β phase. Since the β phase is mechanically less resistant compared to the α phase, its distribution at the grain boundaries can negatively affect the mechanical properties of the material. Fig. 11 (b) shows the detail of the EDX mapping performed in the transition zone of sample 12C for which the P value is 350 W. The transition zone between the AP and the substrate shows a greater segregation of Vanadium-rich phase (phase β) compared to the concentration of beta phase present in the substrate. Such a phase distribution configuration is such that the transition zone, the one enclosed between the red and black dashed lines in Fig. 11 (b), is the low-resistance zone.

3.3. *Numerical simulation of the L-PBF process on the sheet metal: evaluation of residual stresses and displacements in hybrid parts*

The numerical model of the hybrid additive process was used to predict the residual stress after the AM process (see Fig. 12). The experimentally measured values of distortion along the z direction were used to validate the developed numerical model regarding the choice of the scaling factor, i.e., a corrective factor to scale the PRM file and tune the numerical model. Preliminary analyses indicated that decreasing the number of layers per voxel enhances the numerical model's response, although at the cost of increased computational demand. For this reason, a value of 7 layers was used for all the simulations. Fig. 12 (a) shows the predicted distribution of the displacement along the z direction, along with the macrography of the distorted samples for cases 9C, 10C, 11C, and 12C. In Fig. 12 (b), the comparison between the simulated distortions and the measured ones is illustrated for the same case studies. The analysis reveals that the numerical model is able to properly predict the overall trend, with an average error of about 6 %. Figs. 13 and 14 show the longitudinal residual stresses (XX) values obtained from the numerical model. The trends shown in Fig. 13 highlight a distribution of

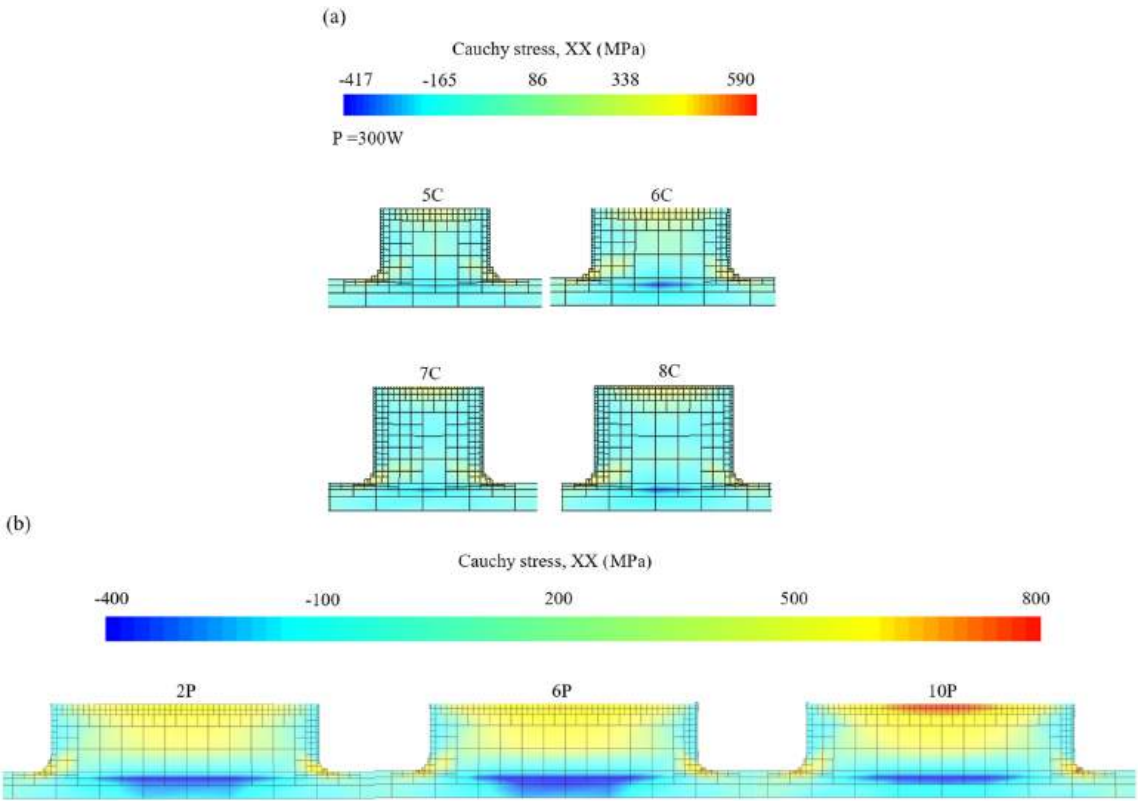

Fig. 13. (a) Longitudinal residual stresses (XX) obtained from the simulation model for cylindrical AP with P = 300W, (b) Longitudinal residual stresses (XX) obtained from the simulation model by varying the laser power for box-shaped AP.

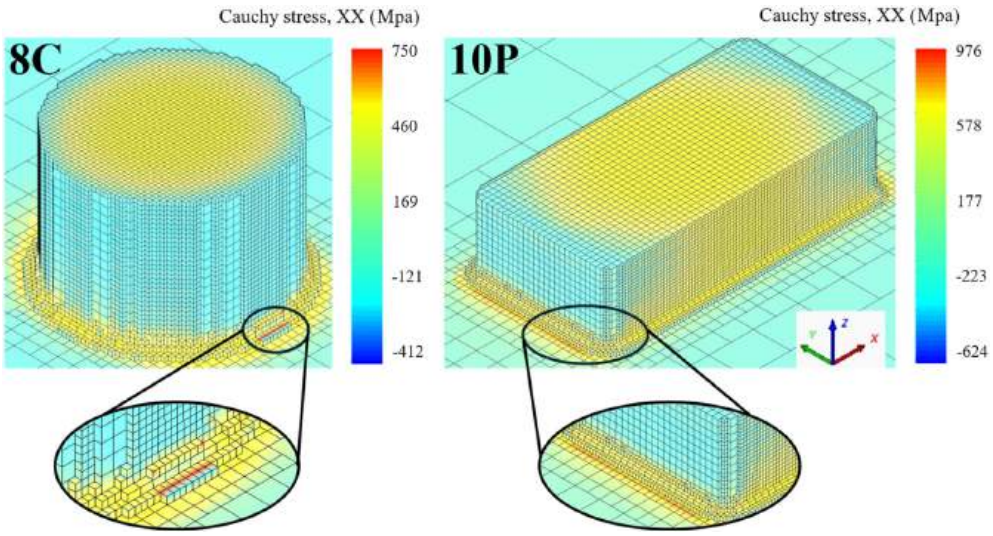

Fig. 14. Longitudinal residual stresses (XX) obtained from the cylindrical and box-shaped AP simulation model.

residual stresses that can explain the interface strength results reported in Fig. 4. For P = 300 W in cylindrical APs, the residual stresses of the samples with higher IS are characterized by a compression zone in the central area of the interface, which justifies the higher recorded resistance observed. In fact, compression residual stress is beneficial when tensile stress is applied through bending. Fig. 14, on the other hand, shows that the numerical model can also highlight the most stressed areas where failure may or in subsequent forming operations. The comparison of Figs. 14 and 9 can also explain the fracture behavior described in the previous paragraphs. In fact, a residual stress concentration is calculated in the fillet area of sample 8C and at the fillet-sheet interface for sample 10P. It is crucial to emphasize that these zones will also experience the highest stresses during any subsequent forming step, such as bending of the sheet metal. This has already been reported by Hafenecker et al. [11] through numerical simulations of the forming process following additive element deposition. Simulations of the additive process aid in predicting mechanical behavior and implementing strategies to mitigate stress concentrations prior to the forming step.

The numerical simulation allows us to justify the observed trends for the sample's distortion (Fig. 7). In Fig. 14, the longitudinal residual stress distribution for samples 2P, 6P, and 10P is shown. The sample 6P, with an intermediate LED value, presents a large compressive zone that

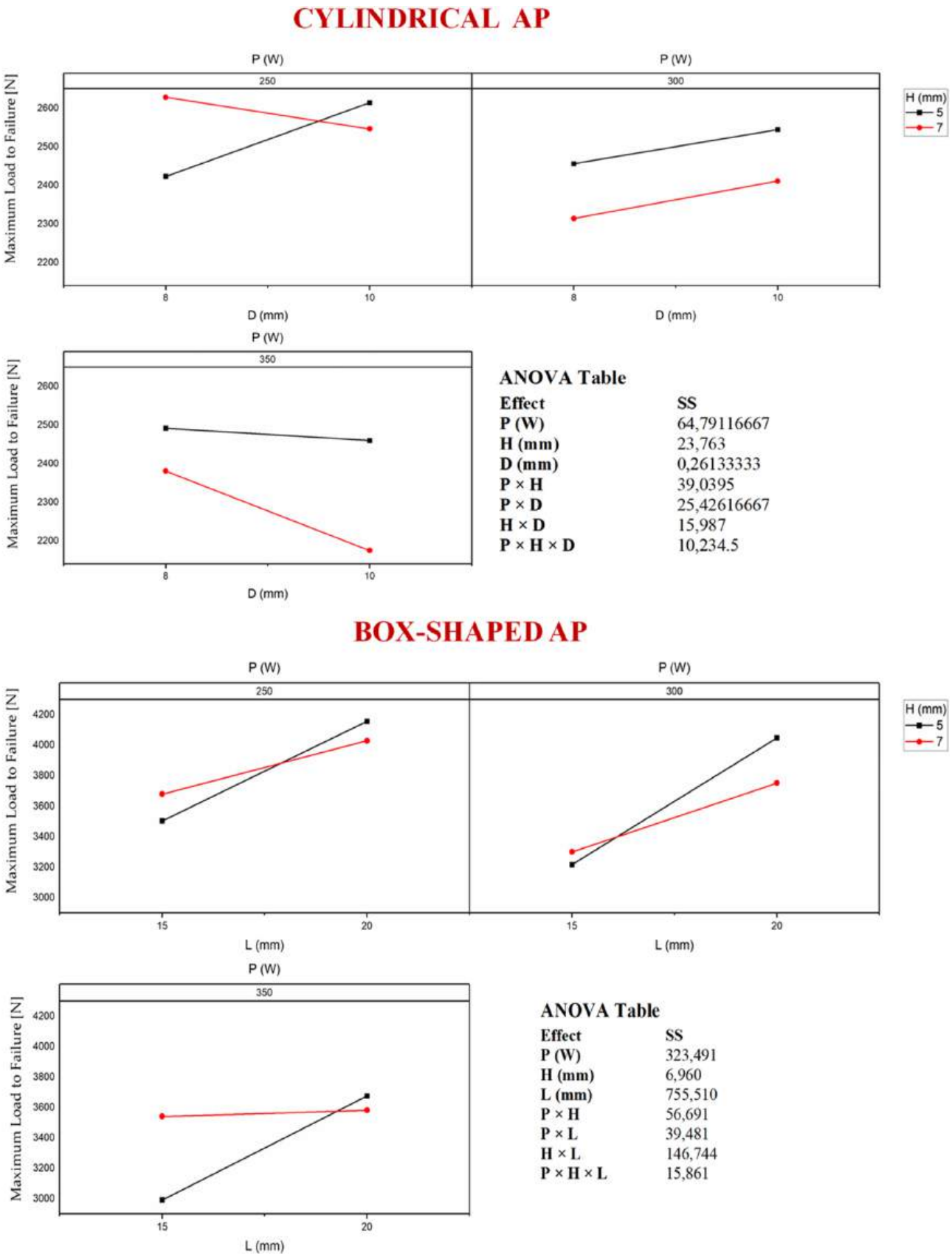

Fig. 15. Three-way ANOVA results for the dependent variable Maximum Load to Failure [N] in three-point bending tests for cylindrical AP and box-shaped AP.

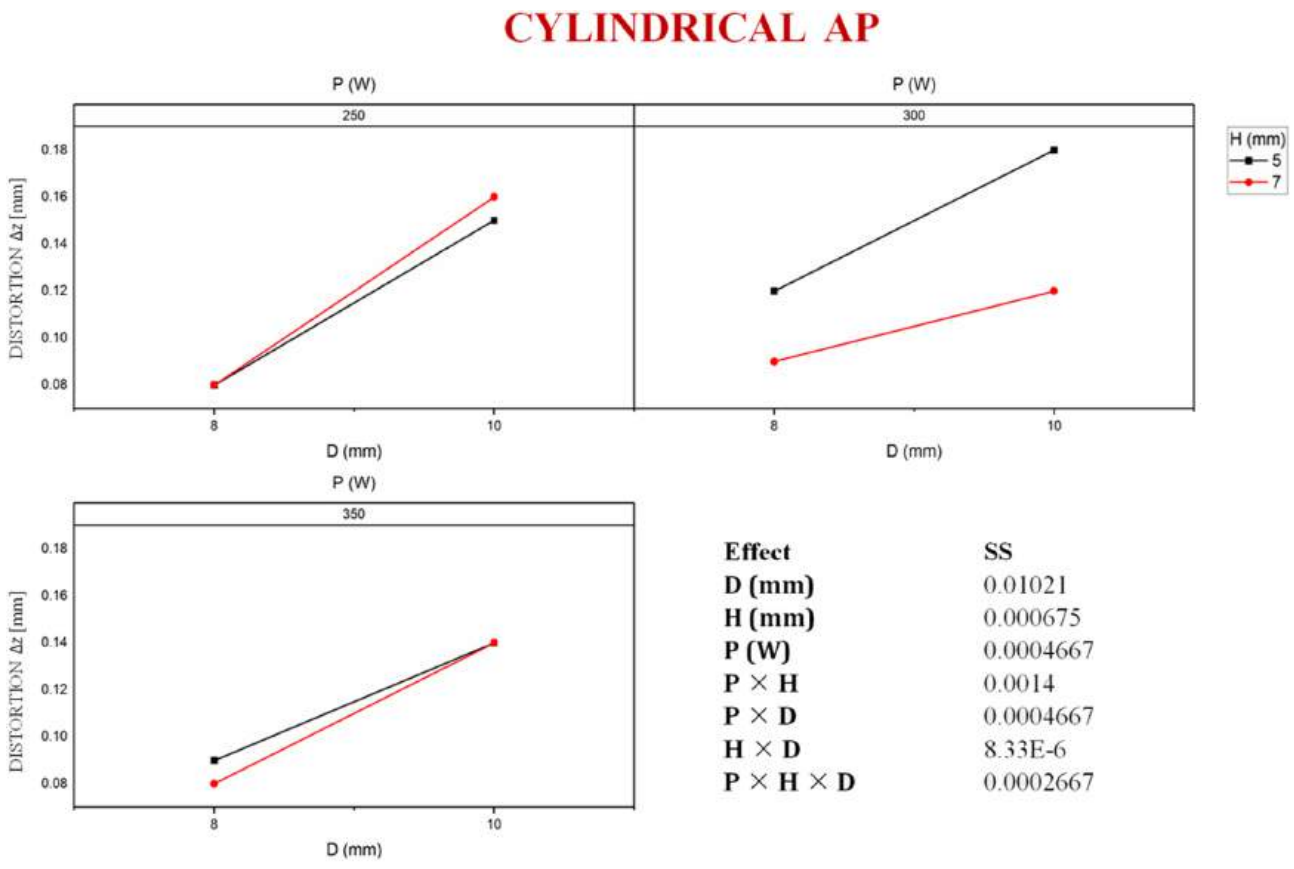

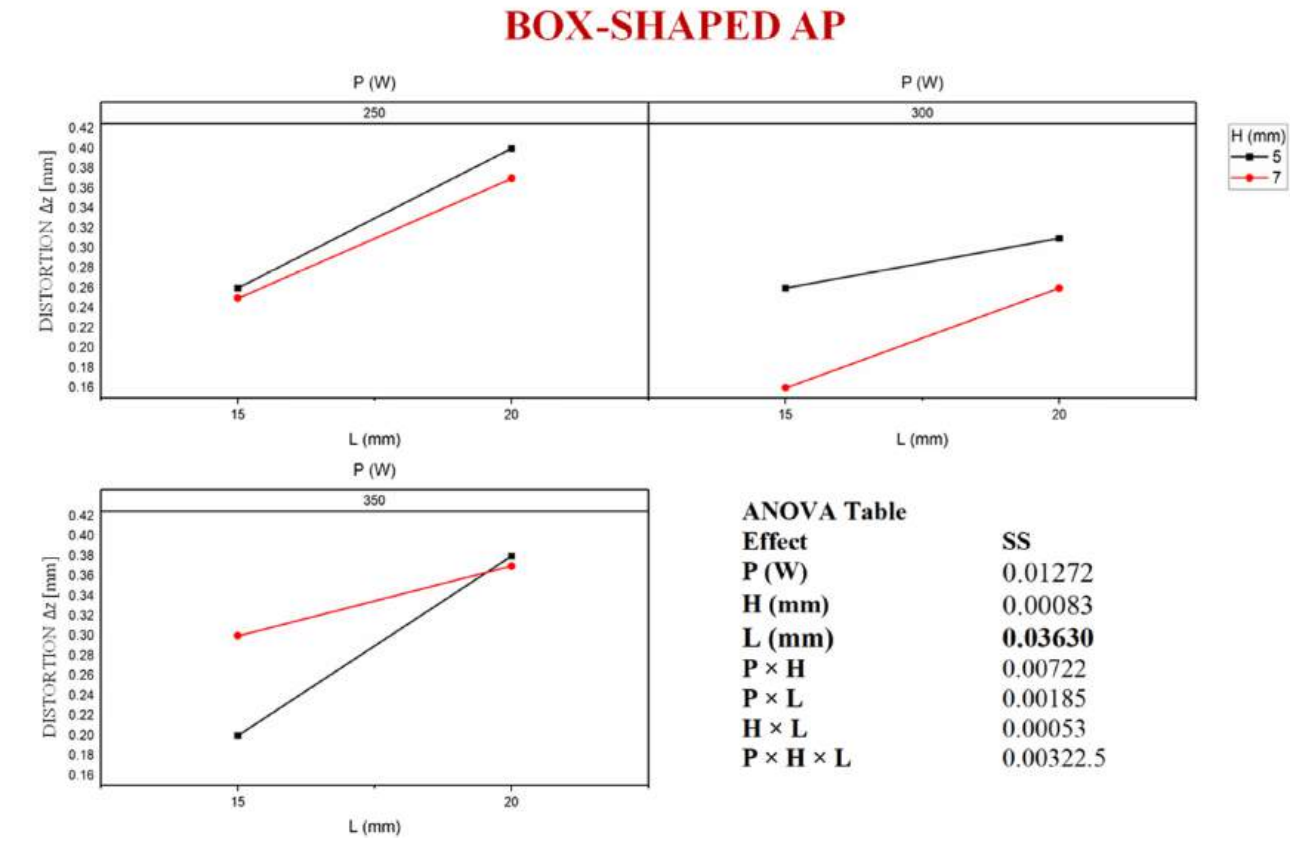

Fig. 16. Three-way ANOVA results for the dependent variable Distortion Δz [mm] in three-point bending tests for cylindrical AP and box-shaped AP.

Table 3
Regression coefficients value for linear and polynomial models.

Coefficients	Linear regression with interactions	Polynomial regression with interactions
a_0	10869	13189
a	−11	−25
b	−98715	−201204
c	−6357	−22340
d	+103	+246
e	+5	+23
f	+76032	+131249
g	–	+0.03
h	–	−1612042
i	–	−134903
l	–	−0.33
m	–	−0.02
n	–	−12008

balances the tensile residual stresses, which are responsible for distortion along the positive z direction. This compressive area is larger than the ones shown by the 2P and 10P samples, which are produced with the lowest and the highest LED values, respectively.

3.4. ANOVA analysis and mathematical model for results generalization

Three-way ANOVA analyses (see Figs. 15 and 16) were conducted to highlight the significant effects of the main technological and geometrical factors, i.e., laser Power, Height of the AP, and Diameter (cylindrical AP) or Length (box-shaped AP) of the parts, as well as their interactions. The results of the analysis are provided in Figs. 15 and 16, both in terms of interaction graphs, to immediately highlight the presence of combined effects, and in numerical terms, highlighting the value of the SS (Sum of Squares) metric. The single or combined effect of the aforementioned main factors was evaluated with respect to the dependent variables represented by bending strength (Fig. 15) and the value of the distortion Δz (Fig. 16). From a graphical viewpoint, the presence of intersecting lines and high values of the SS metric emphasize the strength of double or triple interactions. Intermediate values of the SS metric and converging lines are used to depict double and triple intersections at the medium level. Weak or null interactions are highlighted by parallel lines and low values of the SS metric. The result of the three-way ANOVA for the cylindrical geometry samples and in relation to the bending strength of the transition zone of the AP, shown in Fig. 15, allows stating that the factors P and H are dominant, with the height effect being less marked than that of P. The two-way interactions P × H and P × D are also influential, suggesting that the effects cannot be interpreted independently. Triple interaction is still not negligible. This indicates that the combination of the three factors together has a specific and complex impact on resistance. The result of the three-way ANOVA for the box-shaped geometry samples in relation to the bending strength of the transition zone of the AP, shown in Fig. 15, indicate that the length (L) is the dominant factor in the system, while the Power (P) represents a consistent effect that contributes significantly, although less than L, to the resistance of the AP. Height (H) has a negligible impact and therefore does not significantly influence resistance on its own. From the perspective of double interactions, it is observed that the effect of power changes based on height (and vice versa), and the effect of power partly depends on length. Moreover, the H × L interaction is the strongest of the two-way interactions, indicating that height and length act jointly and generate a significant effect on resistance. The three-way interaction P × H × L is present, but has a marginal impact, meaning that the simultaneous combination of the three factors produces a residual but not dominant effect on resistance. As the distortion Δz is considered, the result of the three-way ANOVA for the cylindrical geometry, shown in Fig. 16, suggests that the diameter D is the predominant factor, and therefore increasing the diameter has a significant impact on distortion. In reference to the double interactions, it is observed that the highest interaction between the double terms occurs between power and height, even if the individual effects are modest. Triple interactions are minimal, so the combined effect of all three factors does not significantly impact distortions. Hence, the optimization of Δz mainly involves controlling the diameter (D). As the box-shaped samples are regarded, the power (P) moderately affects Δz, while height (H) alone does not significantly change Δz. In turn, length (L) significantly impacts distortion along Z. The interactions are generally weak, but P × H is

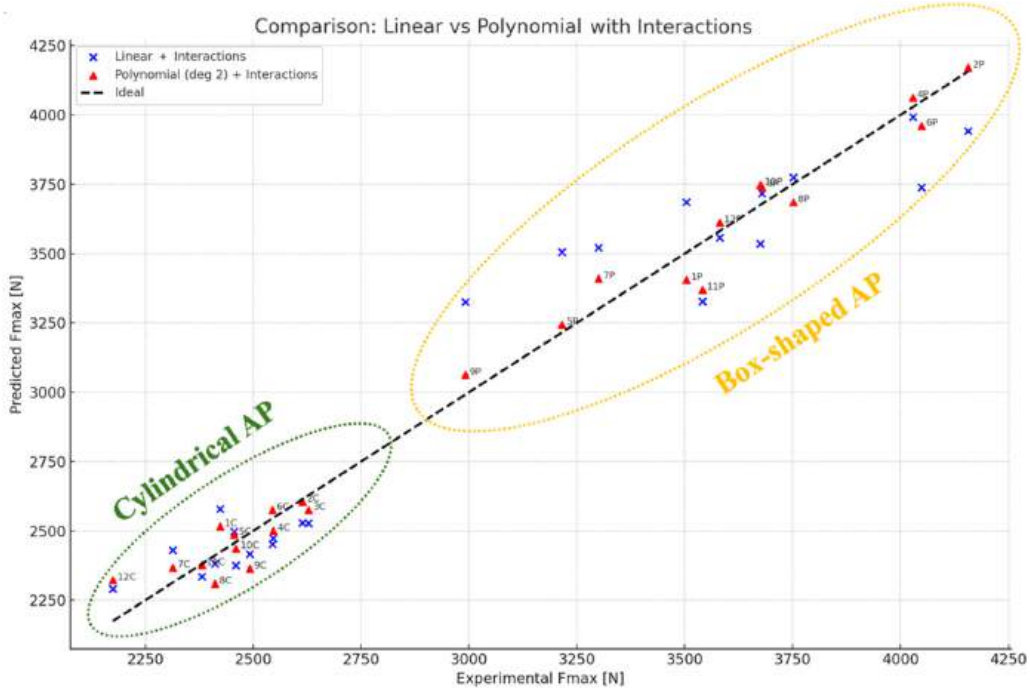

Fig. 17. Comparative graph between the linear regression model with interaction and the degree 2 polynomial regression model with interactions for the evaluation of F_{max} for any geometry.

more relevant than the others. The triple interaction P × H × L, although not dominant, suggests the importance of considering complex combinations in distortion phenomena. Ultimately, the length (L) is the factor that most significantly affects the distortion along the Z-axis, the power (P) has a secondary impact, while the height (H) shows an irrelevant single effect. The ANOVA results highlight significant interactions among key geometrical and process parameters, such as laser power, the height of the additive part (AP), and its extension (diameter for cylindrical AP or length for the box-shaped AP). As a consequence, the effect of each factor cannot be interpreted in isolation, and direct comparisons between individual process conditions or specific samples may become overly simplistic and potentially misleading.

The experimental results and the conducted ANOVA analysis led to the identification of two parameters that characterize the symmetry of the interface surface and the thermal compactness of the additive component. Explicitly, the following two parameters, reported in equations (1) and (2), have been defined to characterize a generic geometry of the APs and define a prediction model for the Fmax resistance independent of the specific geometry. The IoS (eq. (1)) represents an index of the interface surface symmetry (the higher the IoS, the higher the symmetry of the AP) and it is defined as:

$$IoS = \frac{IS}{Per^2} \tag{1}$$

In which *Per* is the Perimeter of the IS, the deposited AM area, or the interface surface. The other parameter is HA_v, an index of heat accumulation, which is reported in eq. (2):

$$HA_v = \frac{IS}{V}\left[mm^{-1}\right] \tag{2}$$

The HA_v is an indicator of the heat accumulation phenomena that occur during the LPBF process, which involves the IS and the volume V of the AP as better specified in Ref. [30].

A linear regression analysis with interactions was then performed following the results obtained from the ANOVA analysis, which indicated significant effects not only of the individual factors but also of the interactions between them. The proposed mathematical model is reported in equation (3):

$$F_{\max} = aP + b\,IoS + c\,HA_v + d\,(P\,IoS) + e\,(P\,HA_v) + f\,(IoS\,HA_v) + a_0 \tag{3}$$

The coefficients of the regression model are shown in Table 3. The proposed linear regression model demonstrated satisfactory performance metrics, achieving an R^2 value of 94 % and an MAE of 127 N. The model comprehensively accounts for the variability in the results obtained. However, a detailed examination of the graph presented in Fig. 17, which depicts the deviation of the Fmax values estimated by the model against the experimental data across all geometries and process parameters, reveals that the proposed model exhibits superior performance with cylindrical geometries in comparison to box geometries, which are characterized by higher Fmax values. This observation suggested refining the regression model by using a 2nd-degree polynomial model, still with interactions. The proposed mathematical model is explicitly shown in equation (4):

$$F_{max} = aP + b\,IoS + c\,HA_V + d\,(P\,IoS) + e\,(P\,HA_V) + f\,(IoS\,HA_V) + gP^2 + h\,(IoS)^2 + i\,(HA_V)^2 + l\,(P\,IoS)^2 + m\,(P\,HA_V)^2 + n\,(IoS\,HA_V)^2 + a_0 \tag{4}$$

The values of the coefficients for the linear, quadratic, and interaction terms are reported in Table 3. The proposed polynomial model, in terms of performance metrics, produced significantly improved values compared to the simple linear model without interactions. Specifically, the R^2 value was calculated to be 98.5 %, and the MAE metric's error decreased, compared to the previous case, now taking on a value of 65 N, meaning the predictions are much closer to the experimental values. The comparison between the linear and polynomial models, shown graphically in Fig. 17, highlights that the newly proposed model significantly increases its degree of geometric generalization, improving the results for the box-shaped APs. The polynomial model performs well regardless of the geometry considered (red triangles closer to the 45-degree line than the blue crosses), making it suitable for use as a decision-making tool during the design phase for selecting geometrical and technological parameters that can guarantee the necessary levels of AP strength.

4. Summary and conclusions

In this work, hybrid components produced by L-PBF on Ti–6Al–4V sheets were systematically characterized to identify the main factors governing the bonding strength at the interface. The study showed that:

- The volumetric energy density, the interface surface (IS), and the symmetry of the deposited additive part jointly control the residual stress distribution and, consequently, the mechanical strength of the hybrid parts;
- An excessive volumetric energy density generally reduces the bonding strength, whereas larger interface surfaces improve heat exchange and cooling, leading to higher interface strength;
- Asymmetric geometries, associated with high length-to-width ratios of the interface, promote residual-stress concentration along the shortest side of the perimeter and reduce the local resistance, as confirmed by microhardness and microstructural analyses.

Building on these results, two geometry-independent parameters were introduced to compactly describe the behavior of the additive part: an interface symmetry index (IoS) and a heat accumulation parameter (HA_V). Finally, a second-degree polynomial model was developed and validated across different geometries, providing a simple and efficient design-support tool for selecting geometric and process parameters that ensure the required bonding strength in hybrid AM components.

These contributions represent a novel framework for quantifying and designing the bonding interface in hybrid AM components, beyond existing studies that mainly address process parameters or single geometries.

Data statement

The authors confirm that the data supporting the findings of this study are available within the article.

Declaration of competing interest

The authors declare that they have no known competing financial interests or personal relationships that could have appeared to influence the work reported in this paper.

Acknowledgements

This study was carried out within the MICS (Made in Italy – Circular and Sustainable) Extended Partnership and received funding from the European Union Next-Generation EU (PIANO NAZIONALE DI RIPRESA E RESILIENZA (PNRR) – MISSIONE 4 COMPONENTE 2,

INVESTIMENTO 1.3 – D.D. 1551.11–10-2022, PE00000004). This manuscript reflects only the authors' views and opinions, neither the European Union nor the European Commission can be considered responsible for them.

References

[1] Liu S, Shin YC. Additive manufacturing of Ti6Al4V alloy: a review. Mater Des 2019; 164. https://doi.org/10.1016/j.matdes.2018.107552.

[2] Blakey-Milner B, Gradl P, Snedden G, Brooks M, Pitot J, Lopez E, et al. Metal additive manufacturing in aerospace: a review. Mater Des 2021;209. https://doi.org/10.1016/j.matdes.2021.110008.

[3] Nouri A, Rohani Shirvan A, Li Y, Wen C. Additive manufacturing of metallic and polymeric load-bearing biomaterials using laser powder bed fusion: a review. J Mater Sci Technol 2021;94:196–215. https://doi.org/10.1016/j.jmst.2021.03.058.

[4] Ligon SC, Liska R, Stampfl J, Gurr M, Mülhaupt R. Polymers for 3D printing and customized additive manufacturing. Chem Rev 2017;117:10212–90. https://doi.org/10.1021/acs.chemrev.7b00074.

[5] Chu W-S, Kim C-S, Lee H-T, Choi J-O, Park J-I, Song J-H, et al. Hybrid manufacturing in micro/nano scale: a review. In J Preci Eng Manufact Green Technol 2014;1:75–92. https://doi.org/10.1007/s40684-014-0012-5.

[6] Shukla M, Todorov I, Kapletia D. Application of additive manufacturing for mass customisation: understanding the interaction of critical barriers. Prod Plann Control 2018;29:814–25. https://doi.org/10.1080/09537287.2018.1474395.

[7] Osman H, Azab A, Hasan R Bin, Baki F. Mass customization using hybrid manufacturing and smart assembly: an optimal configuration and platform design approach. Manuf Lett 2024;41:124–32. https://doi.org/10.1016/j.mfglet.2024.09.016.

[8] Fianko SK, Dzogbewu TC, Agbamava E, de Beer DJ. Mass customisation strategies in additive manufacturing: a systematic review and implementation framework. Processes 2025;13:1855. https://doi.org/10.3390/pr13061855.

[9] Merklein M, Junker D, Schaub A, Neubauer F. Hybrid additive manufacturing technologies – an analysis regarding potentials and applications. Phys Procedia 2016;83:549–59. https://doi.org/10.1016/j.phpro.2016.08.057.

[10] Hafenecker J, Rothfelder R, Schmidt M, Merklein M. Additive and formative manufacturing of hybrid parts with locally adapted. Tailored Properties 2025: 219–40. https://doi.org/10.1007/978-3-031-78350-0_11.

[11] Hafenecker J, Papke T, Merklein M. Influence of stress states on forming hybrid parts with sheet metal and additively manufactured element. J Mater Eng Perform 2021;30:5159–69. https://doi.org/10.1007/s11665-021-05674-8.

[12] Jiménez A, Bidare P, Hassanin H, Tarlochan F, Dimov S, Essa K. Powder-based laser hybrid additive manufacturing of metals: a review. Int J Adv Manuf Technol 2021; 114:63–96. https://doi.org/10.1007/s00170-021-06855-4.

[13] Pragana JPM, Sampaio RFV, Bragança IMF, Silva CMA, Martins PAF. Hybrid metal additive manufacturing: a state–of–the-art review. Adv Ind Manu Eng 2021;2: 100032. https://doi.org/10.1016/j.aime.2021.100032.

[14] Rosenthal S, Hahn M, Tekkaya AE, Platt S, Kleszczynski S, Witt G. Speeding up additive manufacturing by means of forming for sheet components with core structures. Int J Prec Eng Manufact Green Technol 2022;9:1021–34. https://doi.org/10.1007/s40684-021-00384-x.

[15] Ge T, Li Y, Gao D, Yang C, Li F. Hybridizing additive manufacturing and sheet forming process to manufacture complex components with multi-features: a review. J Manuf Process 2024;124:345–64. https://doi.org/10.1016/j.jmapro.2024.06.032.

[16] Dardaei Joghan H, Hahn M, Sehrt JT, Tekkaya AE. Hybrid additive manufacturing of metal laminated forming tools. CIRP Ann 2022;71:225–8. https://doi.org/10.1016/j.cirp.2022.03.018.

[17] Bambach M, Sizova I, Sydow B, Hemes S, Meiners F. Hybrid manufacturing of components from Ti-6Al-4V by metal forming and wire-arc additive manufacturing. J Mater Process Technol 2020;282:116689. https://doi.org/10.1016/j.jmatprotec.2020.116689.

[18] Merklein M, Schulte R, Papke T. An innovative process combination of additive manufacturing and sheet bulk metal forming for manufacturing a functional hybrid part. J Mater Process Technol 2021;291:117032. https://doi.org/10.1016/j.jmatprotec.2020.117032.

[19] Ngo T, Kashani A, Imbalzano G, Nguyen T, Hui D. Additive manufacturing (3D printing): a review of materials, methods, applications and challenges. Compos B Eng 2018;143:25.

[20] Hafenecker J, Bartels D, Kuball C-M, Kreß M, Rothfelder R, Schmidt M, et al. Hybrid process chains combining metal additive manufacturing and forming – a review. CIRP J Manuf Sci Technol 2023;46:98–115. https://doi.org/10.1016/j.cirpj.2023.08.002.

[21] Huber F, Papke T, Kerkien M, Tost F, Geyer G, Merklein M, et al. Customized exposure strategies for manufacturing hybrid parts by combining laser beam melting and sheet metal forming. J Laser Appl 2019;31. https://doi.org/10.2351/1.5096115.

[22] Ambrogio G, Gagliardi F, Muzzupappa M, Filice L. Additive-incremental forming hybrid manufacturing technique to improve customised part performance. J Manuf Process 2019;37:386–91. https://doi.org/10.1016/j.jmapro.2018.12.008.

[23] Lauwers B, Klocke F, Klink A, Tekkaya AE, Neugebauer R, McIntosh D. Hybrid processes in manufacturing. CIRP Ann Manuf Technol 2014;63:561–83. https://doi.org/10.1016/j.cirp.2014.05.003.

[24] Papke T, Hafenecker J, Römisch D, März R, Hentschel O, Bartels D, et al. Alternating additive manufacturing and forming—an innovative manufacturing approach. J Manuf Mater Process 2023;7:90. https://doi.org/10.3390/jmmp7030090.

[25] Chen F, Zha R, Jeong J, Liao S, Cao J. Directed energy deposition on sheet metal forming for reinforcement structures. J Manuf Process 2025;144:339–49. https://doi.org/10.1016/j.jmapro.2025.03.120.

[26] Bambach M, Sviridov A, Weisheit A, Schleifenbaum J. Case studies on local reinforcement of sheet metal components by laser additive manufacturing. Metals 2017;7:113. https://doi.org/10.3390/met7040113.

[27] Hafenecker J, Merklein M. Investigations on sheet metal forming of hybrid parts in different stress states. Prod Eng 2023;17:483–500. https://doi.org/10.1007/s11740-022-01171-6.

[28] Ahuja B, Schaub A, Karg M, Schmidt R, Merklein M, Schmidt M. In: Helvajian H, Piqué A, Wegener M, Gu B, editors. High power laser beam melting of Ti6Al4V on formed sheet metal to achieve hybrid structures; 2015. 93530X. https://doi.org/10.1117/12.2082919.

[29] Schaub A, Ahuja B, Butzhammer L, Osterziel J, Schmidt M, Merklein M. Additive manufacturing of functional elements on sheet metal. Phys Procedia 2016;83: 797–807. https://doi.org/10.1016/j.phpro.2016.08.082.

[30] Palmeri D, Buffa G, Pollara G, Fratini L. Sample building orientation effect on porosity and mechanical properties in selective laser Melting of Ti6Al4V titanium alloy. Mater Sci Eng, A 2022;830. https://doi.org/10.1016/j.msea.2021.142306.

[31] Papke T, Dubjella P, Butzhammer L, Huber F, Petrunenko O, Klose D, et al. Influence of a bending operation on the bonding strength for hybrid parts made of Ti-6Al-4V. Proced CIRP 2018;74:290–4. https://doi.org/10.1016/j.procir.2018.08.113.

[32] Pupillo D, Di Franco F, Palmeri D, Pollara G, Buffa G, Fratini L, et al. Surface treatments on 3D printed Ti6Al4V biomedical plates to enhance corrosion resistance in simulated physiological solutions and under inflammatory conditions. Corros Sci 2024;240:112451. https://doi.org/10.1016/j.corsci.2024.112451.

[33] Costa A, Palmeri D, Pollara G, Fichera S. Multi-objective process parameters optimization of Ti-6Al-4V LPBF parts through a hybrid prediction–optimization approach. Int J Adv Manuf Technol 2025;138:1739–51. https://doi.org/10.1007/s00170-025-15658-w.

[34] Costa A, Buffa G, Palmeri D, Pollara G, Fratini L. Hybrid prediction-optimization approaches for maximizing parts density in SLM of Ti6Al4V titanium alloy. J Intell Manuf 2022;33. https://doi.org/10.1007/s10845-022-01938-9.

[35] Palmeri D, Pollara G, Licari R, Micari F. Finite element method in L-PBF of Ti-6Al-4V: influence of laser power and scan speed on residual stress and part distortion. Metals 2023;13:1907. https://doi.org/10.3390/met13111907.

[36] Gouge M, Michaleris P, Denlinger E, Irwin J. The finite element method for the thermo-mechanical modeling of additive manufacturing processes. In: Thermo-Mechanical modeling of additive manufacturing. Elsevier; 2018. p. 19–38. https://doi.org/10.1016/B978-0-12-811820-7.00003-3.

[37] Peter N, Pitts Z, Thompson S, Saharan A. Benchmarking build simulation software for laser powder bed fusion of metals. Addit Manuf 2020;36:101531. https://doi.org/10.1016/j.addma.2020.101531.

[38] Farina I, Fabbrocino F, Carpentieri G, Modano M, Amendola A, Goodall R, et al. On the reinforcement of cement mortars through 3D printed polymeric and metallic fibers. Compos B Eng 2016;90:76–85. https://doi.org/10.1016/j.compositesb.2015.12.006.

[39] Li T, Wang L. Bending behavior of sandwich composite structures with tunable 3D-printed core materials. Compos Struct 2017;175:46–57. https://doi.org/10.1016/j.compstruct.2017.05.001.

[40] Palmeri D, Buffa G, Pollara G, Fratini L. The effect of building direction on microstructure and microhardness during selective laser melting of Ti6Al4V titanium alloy. J Mater Eng Perform 2021. https://doi.org/10.1007/s11665-021-06039-x.